


Article

Controllable Fabrication of Heterogeneous p-TiO₂ QDs@g-C₃N₄ p-n Junction for Efficient Photocatalysis

Songbo Wang ^{1,2} , Feifan Wang ¹, Zhiming Su ¹, Xiaoning Wang ¹, Yicheng Han ¹, Lei Zhang ¹, Jun Xiang ¹, Wei Du ¹ and Na Tang ^{1,*}

¹ Tianjin Key Laboratory of Brine Chemical Engineering and Resource Eco-utilization, College of Chemical Engineering and Materials Science, Tianjin University of Science & Technology, Tianjin 300457, China; wangsongbo@tust.edu.cn (S.W.); wangfeifan4500@sina.com (F.W.); suzhiming0321@sina.com (Z.S.); wangxiaoning@sina.com (X.W.); hanyicheng1998@sina.com (Y.H.); Leizhang@tust.edu.cn (L.Z.); jxiang@tust.edu.cn (J.X.); duwei@tust.edu.cn (W.D.)

² Tianjin Key Laboratory of Marine Resources and Chemistry, Tianjin University of Science & Technology, Tianjin 300457, China

* Correspondence: tjtangna@tust.edu.cn; Tel./Fax: +86-22-60602745

Received: 4 April 2019; Accepted: 6 May 2019; Published: 10 May 2019



Abstract: Photocatalytic technology has been considered to be an ideal approach to solve the energy and environmental crises, and TiO₂ is regarded as the most promising photocatalyst. Compared with bare TiO₂, TiO₂ based p-n heterojunction exhibits a much better performance in charge separation, light absorption and photocatalytic activity. Herein, we developed an efficient method to prepare p-type TiO₂ quantum dots (QDs) and decorated graphitic carbonitrile (g-C₃N₄) nanocomposites, while the composition and structure of the TiO₂@g-C₃N₄ were analyzed by X-ray diffraction, Fourier transform infrared spectroscopy, thermogravimetric analysis, transmission electron microscopy, X-ray photoelectron spectroscopy and UV-visible diffuse reflectance spectroscopy characterizations. The characterization results reveal the surface decorated TiO₂ quantum dots is decomposed by titanium glycerolate, which exhibits p-type conductivity. The presence of p-n heterojunction over interface is confirmed, and photoluminescence results indicate a better performance in transfer and separation of photo-generated charge carriers than pure semiconductors and type-II heterojunction. Moreover, the synergy of p-n heterojunction over interface, strong interface interaction, and quantum-size effect significantly contributes to the promoted performance of TiO₂ QDs@g-C₃N₄ composites. As a result, the as-fabricated TiO₂ QDs@g-C₃N₄ composite with a p/n mass ratio of 0.15 exhibits improved photo-reactivity of 4.3-fold and 5.4-fold compared to pure g-C₃N₄ in degradation of organic pollutant under full solar spectrum and visible light irradiation, respectively.

Keywords: p-n heterojunction; g-C₃N₄; TiO₂; charge separation; photocatalysis

1. Introduction

With the increasing concerns regarding the global environmental and energy-related crises over the past decades, photocatalytic technology has been considered to be an effective approach since the foundation of Fujishima-Honda effect in 1972 [1,2]. The key for an efficient photocatalytic process lies in the design and construction of highly active photocatalyst, which requires a wide light absorption edge, fast transfer and separation of photo-generated charge carriers, and quick surface redox reaction [3–7]. TiO₂ is regarded as the most promising photocatalyst due to the advantages such as earth abundance, low price, excellent thermal and chemical stability, and being environmentally friendly [8,9]. Unfortunately, the broad band gap (i.e., 3.2 eV for anatase) means TiO₂ can only be excited by ultraviolet (UV) light, which is less than 5% in the solar spectrum. Meanwhile, the fast

charge recombination rate in single TiO₂ also results in a low quantum efficiency. Therefore, it is an urgently necessary to promote the light absorption and charge separation efficiency of TiO₂ to meet the requirements of industrial applications [10,11].

Recently, many researchers have focused on the modification of TiO₂ towards an improved photocatalytic performance, including for: morphology modulation [12–14], metal or nonmetal doping [15–18], defect engineering [19–22], and fabrication of hetero/homojunction [2,23–27]. In our previous reports, we found that the introduction of titanium vacancies into TiO₂ will widen the valence band, which controls the mobility of holes inherently and thus increase charge separation efficiency. Moreover, the introduction of metal vacancies can alter TiO₂ from an n-type semiconductor to a p-type semiconductor [28]. Pan et-al. modified p-type TiO₂ with n-type TiO₂ quantum dots (QDs) to construct p-n homojunction, and the resulted p-n homojunction exhibits significantly high photo-activity compared with pure type TiO₂, which is attributed to the formation of large electronic field over the interface [29]. Moreover, besides the influence of p-n homojunction, quantum sized TiO₂ can also enhance the charge separation due to the quantum size effect [13,30–32]. However, in these reports, both the titanium defected TiO₂ and TiO₂ QDs still absorb only UV light, which limits their applications under sunlight.

Graphic carbon nitride (g-C₃N₄) is a promising metal-free photocatalyst in the field of H₂ production, organic pollutant degradation, CO₂ reduction, and artificial photosynthesis due to the suitable band structure (2.7~2.8 eV), excellent chemical and thermal stability [33–37]. Usually, g-C₃N₄ is synthesized by thermal condensation of melamine, urea or other triazine derivatives, but the resultant product exhibits an irregular 2D aggregation structure, leading to a lower surface area and electrical conductivity, as well as an increased charge carrier recombination [38,39]. Both theoretical and experimental results suggest that nanosheet structured g-C₃N₄ will exhibit a larger surface area and lower charge transfer resistance, so the exfoliation of bulk g-C₃N₄ into nanosheets has been regarded as an effective approach to promote the photocatalytic performance of g-C₃N₄ [40,41]. Wang et-al. applied a liquid exfoliation method on bulk g-C₃N₄ to prepare layer g-C₃N₄, and the charge transfer resistance decreased by 75% according to the electrochemical impedance spectroscopy (EIS) results, indicating a lower charge recombination [42]. Cheng et-al. conducted an exfoliation treatment on bulk g-C₃N₄ using a simple thermal oxidation etch method, and g-C₃N₄ nanosheets with layer thickness of 2 nm and surface area of 306 m²/g were obtained. Compared with bulk g-C₃N₄, the charge carrier life in the as-prepared g-C₃N₄ nanosheets is prolonged because of the quantum confinement effect [43]. Li and coworkers also reported the synthesizing of 6–9 atomic thick g-C₃N₄ nanosheets by a thermal exfoliation approach, the photocatalytic degradation rate is 2.9 times higher than that of bulk g-C₃N₄ [44]. Therefore, the exfoliation of bulk g-C₃N₄ to nanosheets can effectively increase the surface area, and thus improve charge transfer and separation.

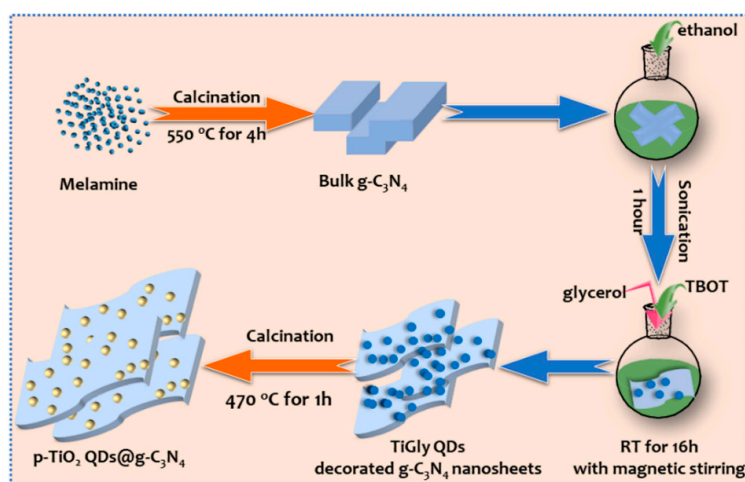
Construction of heterojunction is an effective approach to improve the photocatalytic performance by combining both the advantage of two semiconductors, and the electronic field will enhance the charge transfer and separation across the interface. Type II heterojunction with staggered band alignment is the most widely studied structure. Jiang et-al. placed 5.5 nm sized TiO₂ on g-C₃N₄ nanosheets. Due to the formation of type-II heterojunction, the resultant composites exhibited a Rhodamine B (RhB) degradation rate of 2.5-fold compared to pure g-C₃N₄ [25]. However, this is due to the fact that the work function of the same types semiconductor is closed to each other, which limits the driving force in type-II heterojunction. Instead, with different conductivity types semiconductor contacts, p-n heterojunction will be formed and the difference of the work function is large enough to realize a more efficient charge carrier separation [26,29]. For example, Wang et-al. reported that Cu₂O/TiO₂ p-n junction exhibits a much better photoelectrochemical activity than that of pure TiO₂ and pure Cu₂O [27].

In this work, based on the improvement of our previous work [26,28,29], nanosized titanium glycerolate (TiGly), precursors of p-type TiO₂ quantum dots, were successfully synthesized and in-situ deposited on the surface of g-C₃N₄. TiO₂@g-C₃N₄ nanosheet p-n heterojunctions were then obtained after calcination in air. This p-n junction can achieve the function of killing three birds with one stone: p-type TiO₂ QDs for promoted charge separation, g-C₃N₄ nanosheets for lower charge resistance and p-n junction for enhanced charge transfer over interface. Therefore, compared with pure g-C₃N₄

and $\text{TiO}_2/\text{g-C}_3\text{N}_4$ type-II heterojunction, TiO_2 QDs@ $\text{g-C}_3\text{N}_4$ p-n heterojunctions exhibit promoted electron-hole separation efficiency and excellent photocatalytic performance in degradation of organic pollutant and hydrogen evolution.

2. Results and Discussion

The synthesizing process of bulk $\text{g-C}_3\text{N}_4$ and TiO_2 @ $\text{g-C}_3\text{N}_4$ p-n heterojunctions were diagrammatically presented in Scheme 1. Consistent with the literature reported, melamine was calcined in air at 550°C and then bulk $\text{g-C}_3\text{N}_4$ were obtained. Previously, we have demonstrated that titanium glycerolate (TiGly) is the precursor of p-type TiO_2 , the organic groups will be gradually removed after calcination, and titanium vacancies (V_{Ti}) will be introduced into TiO_2 during the conjunction process of the remaining Ti-O-Ti parallel lattice chains. Herein, in order to fabricate TiO_2 @ $\text{g-C}_3\text{N}_4$ p-n heterojunction, bulk $\text{g-C}_3\text{N}_4$ is synthesized firstly, and then TiGly nanoparticles were in-situ deposited on the surface of $\text{g-C}_3\text{N}_4$ and labeled as TGC- x according to the added $\text{g-C}_3\text{N}_4$. After calcination in air, $\text{g-C}_3\text{N}_4$ was exfoliated and TiGly nanoparticles were decomposed to p-type TiO_2 QDs (labeled as PTC- x). The sharp peak at about 27.4° in the X-ray diffraction (XRD) pattern of TGC- x (Figure 1a) can be attributed to the periodic accumulation of layers of conjugated aromatic systems in bulk $\text{g-C}_3\text{N}_4$ [45]. In the sample TGC-20 and TGC-40, a weak peak appearing at about 10.2° , which is the characteristic peaks corresponding to TiGly [28], indicating the presence of TiGly nanoparticles. As for TGC-60, the content of TiGly is too low to be detected.



Scheme 1. Schematic fabrication procedures of $\text{g-C}_3\text{N}_4$ and TiO_2 @ $\text{g-C}_3\text{N}_4$ p-n heterojunctions.

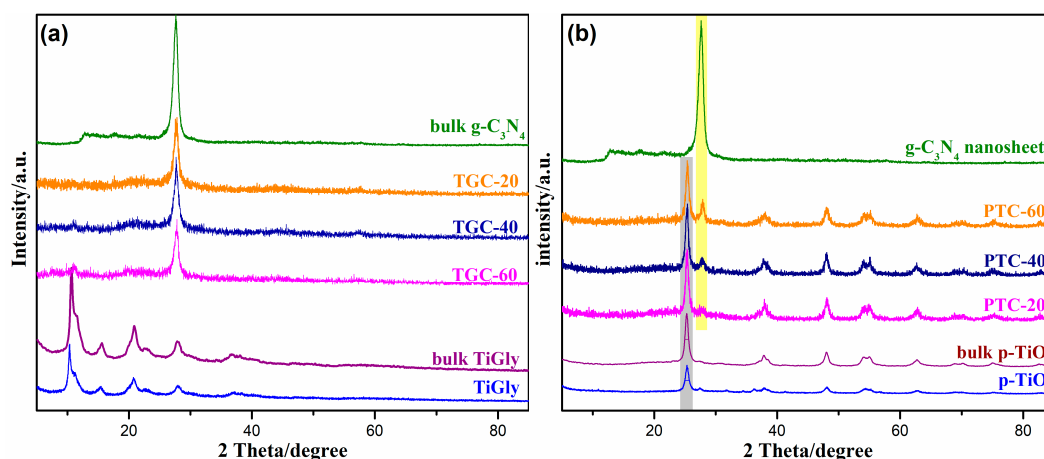
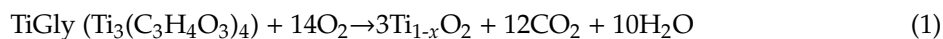


Figure 1. (a) XRD pattern of bulk $\text{g-C}_3\text{N}_4$, bulk and nanoparticle TiGly and TGC- x before calcination; (b) XRD pattern of $\text{g-C}_3\text{N}_4$ nanosheets, bulk and nanoparticle p- TiO_2 and PTC- x after calcination.

After being calcined at 470 °C for 1 h, TiGly nanoparticles will be decomposed into anatase p-type TiO₂. As shown in Figure 1b, no diffraction peaks of TiGly can be observed, only anatase TiO₂ (JCPDS No. 21-1272) and g-C₃N₄ (JCPDS No. 87-1526) can be observed in PTC-*x*, with no other visible phases or impurities. Notably, the full-width at half maxima (FWHM) of peaks at 25.3° corresponding to (101) planes of p-type TiO₂ nanoparticles is broadened from 0.57 to 0.65 compared with bulk p-TiO₂, so the average particle size of the TiO₂ nanoparticles is smaller than the bulk p-TiO₂ according to Scherer Equation. The same phenomenon can also be observed in bulk g-C₃N₄ and g-C₃N₄ nanosheets, the peak at 27.4° corresponding to (002) plane of g-C₃N₄ nanosheets is broadened and drastically weakened from PTC-60 to PTC-20, which is due to the decreased thickness of nanosheets during the thermal exfoliation process [39]. Moreover, we also calculated the lattice constant of the p-type TiO₂ nanoparticles based on XRD patterns, the results indicate that *a* = *b* = 3.793 Å, slightly larger than normal anatase TiO₂ (*a* = *b* = 3.785 Å for JCPDS No. 21-1272), whereas the *c* axis shrinks from 9.514 Å to 9.488 Å, which is identical with that of titanium defected TiO₂ [28].

Thermogravimetric (TG) tests were conducted to quantify the relative content of TiO₂ QDs in the as-prepared samples. As shown in Figure 2, the weight loss of the samples below 80 °C is due to the removal of surface absorbed water, whereas the weight loss between 80 °C and 400 °C is attributed to the decomposition of titanium glycerolate as shown in Equation (1) [28,29]. Since bulk g-C₃N₄ exhibits almost no weight loss in this range, the weight loss of TGC-*x* can all assigned to the decomposition of TiGly. As shown in Figure 2, the weight loss is 20.03%, 9.77% and 7.98% for TGC-20, TGC-40 and TGC-60, respectively. Therefore, according to Equations (2) and (3), the mass content of TiGly in TGC-*x* can be calculated as 43.7%, 21.3% and 17.4%, respectively, corresponding to a p-type TiO₂ QDs mass content of 29.6%, 12.8% and 10.2% in PTC-20, PTC-40 and PTC-60, respectively. Additionally, there is a slight weight increase after 80 °C for all the samples, which may be due to the impurity in the sample gas used in TG tests, but this deviation will not affect the calculated QDs content in the samples.



$$y_{\text{TG}} = \frac{W_s}{W_{\text{TG}}} \quad (2)$$

$$y_{\text{TiO}_2} = \frac{m_{\text{TiO}_2}}{m_{\text{TiO}_2} + m_{\text{g-C}_3\text{N}_4}} = \frac{y_{\text{TG}}(1 - W_{\text{TG}})}{y_{\text{TG}}(1 - W_{\text{TG}}) + 1 - y_{\text{TG}}} = \frac{y_{\text{TG}} - y_{\text{TG}}W_{\text{TG}}}{1 - y_{\text{TG}}W_{\text{TG}}} \quad (3)$$

Among these figures: y_{TG} is the calculated content of TiGly, %; W_s is the weight loss of TGC-*x*, %; W_{TG} is the weight loss of pure TiGly, %; m_{TiO_2} is the calculated mass of TiO₂ in unit mass of PTC-*x*, g; $m_{\text{g-C}_3\text{N}_4}$ is the calculated mass of g-C₃N₄ in unit mass of PTC-*x*, g; y_{TiO_2} is the calculated mass content of p-type TiO₂ QDs in PTC-*x*, %.

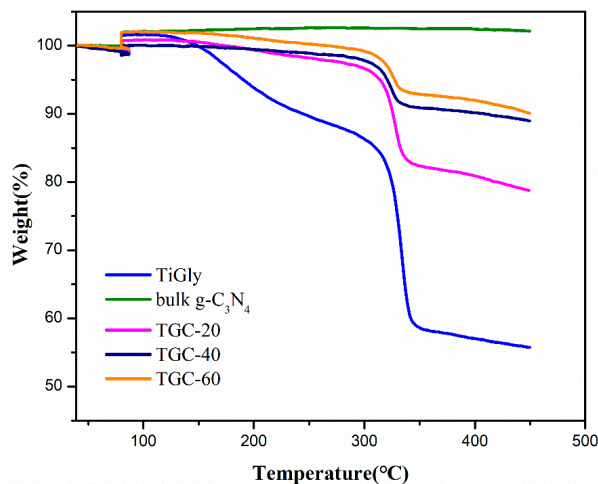


Figure 2. TG profiles of bulk g-C₃N₄, TiGly and TGC-*x*.

High resolution transmission electron microscopy (HRTEM) analyses were conducted to reveal the morphology and composition of the samples. Unlike the densely packed bulk $g\text{-C}_3\text{N}_4$ reported in literatures [39], the as-prepared $g\text{-C}_3\text{N}_4$ exhibits a nanosheet structure, the edges are curled and rough due to the minimizing surface energy (Figure 3a), which provides a lower resistance pathway for charge transfer. As shown in Figure 3b–d, the light contrast nanosheets are $g\text{-C}_3\text{N}_4$ nanosheets whereas the dark contrast are the p-type TiO_2 nanoparticles decomposed from TiGly. Figure 3e shows the lattice fingers of 0.35 nm and 0.48 nm in the dark contrast, corresponding to the (101) and (002) planes of anatase TiO_2 , which reveal the exposure of (010) facet of anatase, consistent with the XRD results [31]. The typical size of TiO_2 nanoparticles is 4–5 nm according to the particle size distribution result shown in the inset of Figure 3e, which is accordance with the characteristic size of quantum confinement effect. It is noteworthy that when the p-type TiO_2 QDs are in-situ grown on the surface of $g\text{-C}_3\text{N}_4$, there is a strong interaction that exists between them so that the TiO_2 QDs cannot be peeled off even after a 30 min ultra-sonication process. Moreover, the strong interaction implies an obvious interface heterojunction between TiO_2 QDs and $g\text{-C}_3\text{N}_4$, which will enhance the transfer of photo generated electrons and holes [25]. In addition, in agreement with the TG results, the relative content of TiO_2 QDs decreases from PTC-20 to PTC-60.

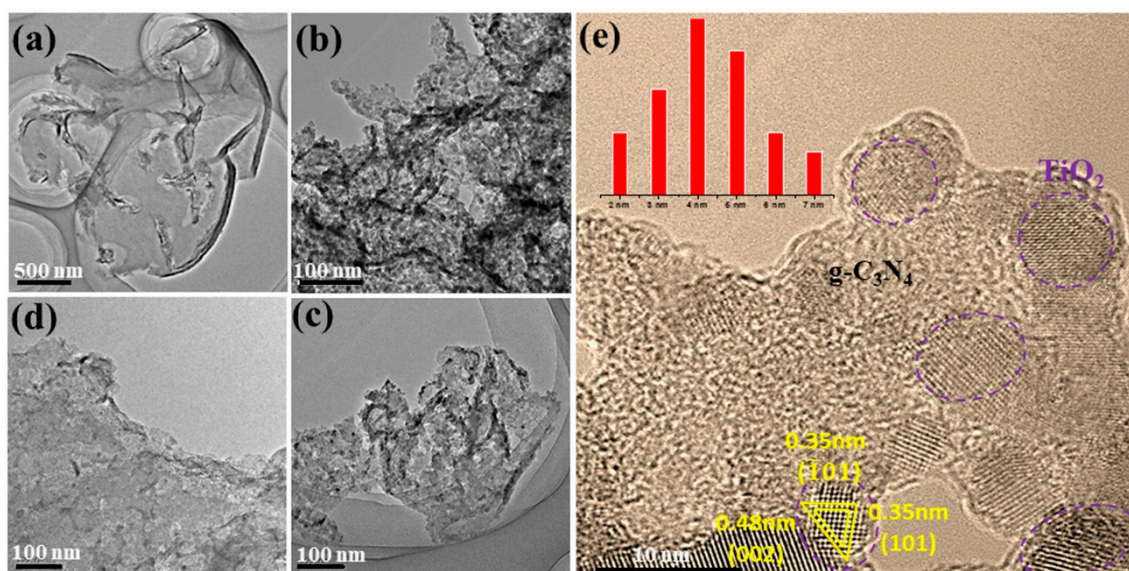


Figure 3. TEM images of (a) $g\text{-C}_3\text{N}_4$ nanosheets, (b) PTC-20, (c) PTC-40 and (d) PTC-60, (e) is the enlarged image of PTC-40, inset: size distribution of TiO_2 QDs in PTC-40.

In order to further investigate the composition and interaction between p-type TiO_2 QDs and $g\text{-C}_3\text{N}_4$ in the as-prepared composites, Fourier transform infrared spectroscopy (FT-IR) and X-ray photoelectron spectroscopy (XPS) characterizations were conducted. As shown in Figure 4a, for the TGC- x , there are three characteristic bands corresponding to $g\text{-C}_3\text{N}_4$, namely the broad peaks located at $3000\text{--}3400\text{ cm}^{-1}$ assigned to the stretching of N–H bonds, the strong peaks at $1250\text{--}1650\text{ cm}^{-1}$ due to the stretching vibration of C=N heterocycles and C–N bonds, and the band around 808 cm^{-1} related to the ring vibration of s-triazine [45–48]. Moreover, besides the above three peaks, another three peaks related to TiGly appearing in TGC- x , the peaks located at around $1000\text{--}1150\text{ cm}^{-1}$ were attributed to the alcoholic Ti–O–C stretching mode, the apparent peak at 611 cm^{-1} was indexed to the stretching mode of Ti–O bonds, and the bands located at $2855\text{--}2927\text{ cm}^{-1}$ were assigned to the glycerol C–H stretching vibration [49]. Besides, the broad peak over $3000\text{--}3600\text{ cm}^{-1}$ was attributed to the presence of physically adsorbed water and glycerol O–H stretching mode. Therefore, by combining with the XRD, TG and FT-IR results, it is proved that the as-prepared TGC- x samples is composed by TiGly and $g\text{-C}_3\text{N}_4$.

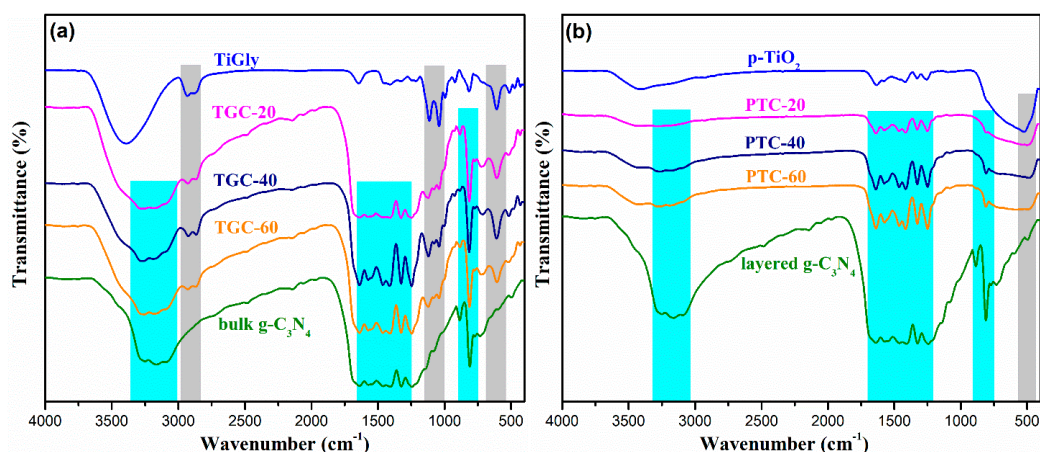


Figure 4. (a) FT-IR patterns of bulk $g\text{-C}_3\text{N}_4$, TiGly and TGC- x before calcination; (b) FT-IR patterns of layered $g\text{-C}_3\text{N}_4$, $p\text{-TiO}_2$ and PTC- x .

Upon calcination, the major FT-IR peaks of $g\text{-C}_3\text{N}_4$ almost all remained in PTC- x samples (Figure 4b). However, the bands assigned to C–H and O–H in TiGly disappeared, while only the stretching band of Ti–O remained, indicating the transformation of TiGly to TiO_2 , further confirming the formation of TiO_2 QDs@ $g\text{-C}_3\text{N}_4$ heterojunction. Moreover, with the decrement of $g\text{-C}_3\text{N}_4$ content from PTC-60 to PTC-20, the intensity of s-triazazine ring vibration 808 cm^{-1} also decreases, which is in agreement with the above TG results. It is noteworthy that the stretching vibration of Ti–O–Ti shifted significantly towards a lower wavenumber in PTC- x composites, suggesting a strong interaction exists between $p\text{-TiO}_2$ QDs and $g\text{-C}_3\text{N}_4$ [25], which is in favor of charge transfer across the interface and thus promotes the photocatalytic performance of the heterojunction.

XPS spectra were recorded to study the status of the C, N, Ti and O elements in the composites. Figure 5a shows the C1s XPS spectra of the samples, there are two main peaks located at 284.8 eV and 288.5 eV, respectively. The peak located at higher binding energy is attributed to the sp^3 -bonded C of N-C=N_2 in $g\text{-C}_3\text{N}_4$, and the peak located at 284.8 eV is due to the surface contaminated carbon during XPS test and sp^2 -hybridized carbon atoms presented in graphic domains [29]. In the N1s XPS spectra (Figure 5b), an asymmetric profile can be observed in all the samples, with a main peak at 401 eV and a shoulder peak at lower binding energy, the main peak is due to the sp^2 -hybridized nitrogen (C–N–C), while the shoulder peak is usually attributed to amino functional groups with a hydrogen atom (C–NH) and sp^3 -hybridized nitrogen (N–[C]3) [25,39]. For the Ti 2p XPS spectra of the PTC- x (Figure 5c), the binding energy of Ti $2p_{3/2}$ and Ti $2p_{1/2}$ are observed at 458.9 eV and 464.4 eV, respectively, suggests the existence of TiO_2 in the samples. Notably, compared with the Ti 2p binding energy of 458.4 eV in n-type TiO_2 [29], the Ti 2p binding energy in the as-prepared samples shifted towards a higher binding energy, indicating the existence of titanium vacancies (V_{Ti}) and p-type properties of the TiO_2 QDs [28].

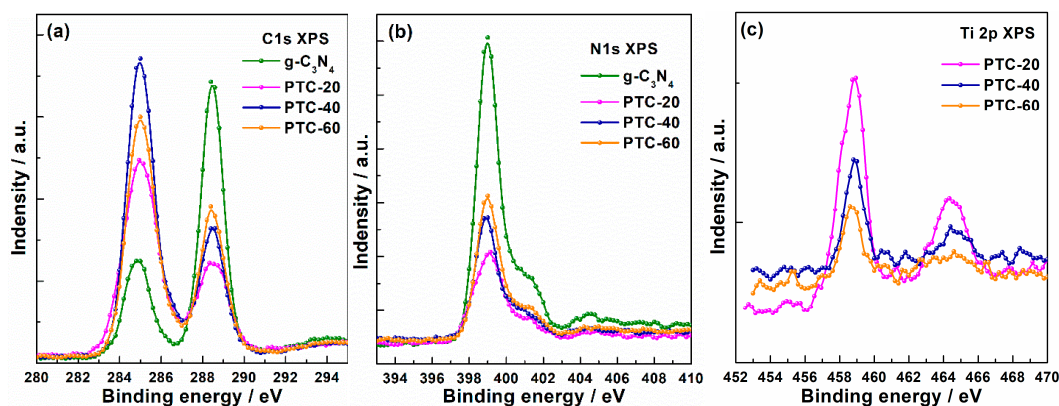


Figure 5. (a) C1s, (b) N1s and (c) Ti 2p XPS spectra of layered $g\text{-C}_3\text{N}_4$, $p\text{-TiO}_2$ and PTC- x , respectively.

The O1s XPS spectra are shown in Figure 6, there is only one symmetrical peak at around 532.7 eV appearing in pure g-C₃N₄, which is attributed to the loosely bonded oxygen species on the surface (O₂, H₂O or OH groups), no peaks corresponding to C–O and N–C–O appeared at 531.4 eV, indicating that no O doping process occurred in g-C₃N₄ during the calcination process [38]. As for the TiO₂@g-C₃N₄ composites, the O1s peaks split into two peaks located at 532.7 eV and 529.8 eV, respectively. The lower binding energy is assigned to the oxygen anions (O²⁻) in the crystal lattice of anatase [28], and the concentration of TiO₂ QDs is proportional to the intensity of this peak. As shown in Figure 6b–d, from PTC-20 to PTC-60, the intensity of this peak becomes obviously weak, confirming the gradually decreased content of TiO₂ QDs in the composites. These results are in good agreement with the TEM, TG and FT-IR results, indicating that the composites are composed of g-C₃N₄ and p-type TiO₂ QDs, and that the content of TiO₂ QDs decreases from PTC-20 to PTC-60.

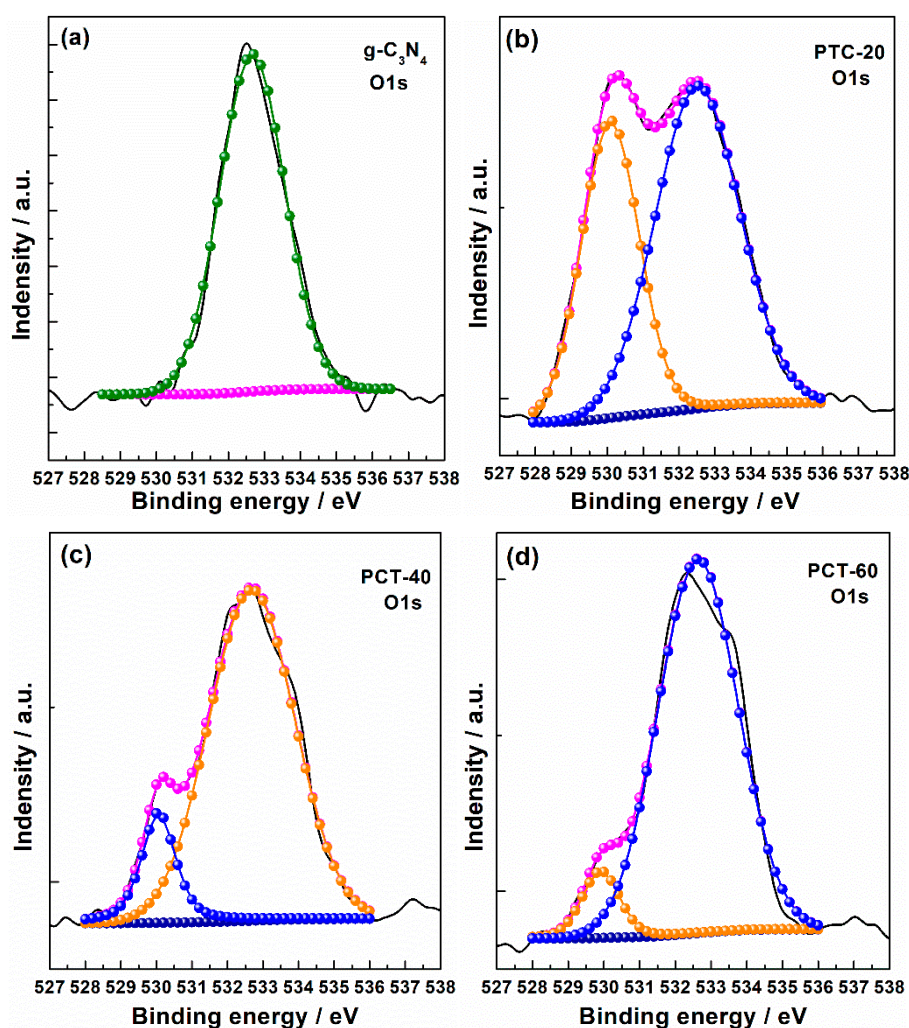


Figure 6. Fitted O1s XPS spectra of (a) layered g-C₃N₄, (b) PTC-20, (c) PTC-40 and (d) PTC-60, respectively.

The light absorption properties of the as-prepared samples were characterized by UV-visible diffuse reflection spectrum (UV-vis DRS). As illustrated in Figure 7a, pure g-C₃N₄ can absorb light from UV region to visible light up to 465 nm, while p-type TiO₂ only absorb UV light up to 400 nm. As for the TiO₂ QDs@g-C₃N₄ composites, there is a remarkable absorption edge extension to the visible region compared with single TiO₂ [39]. Moreover, with the increasing content of g-C₃N₄ from PTC-20 to PTC-60, the optical absorption edge of p-n heterojunction shifts towards a longer wavelength, indicating a stronger light absorption in the visible light region, which is beneficial for the improvement of photocatalytic performance. Meanwhile, the quantum-size effect of the p-type TiO₂

QDs is illustrated by VB XPS spectra. As shown in Figure 7b, a blue shift of VB edge is observed in the as-prepared heterojunctions due to the existence of TiO₂ nanoparticles, and this tendency becomes more and more obvious with the increment of TiO₂, confirming the quantum dots nature of the surface decorated p-type TiO₂ nanoparticles [31].

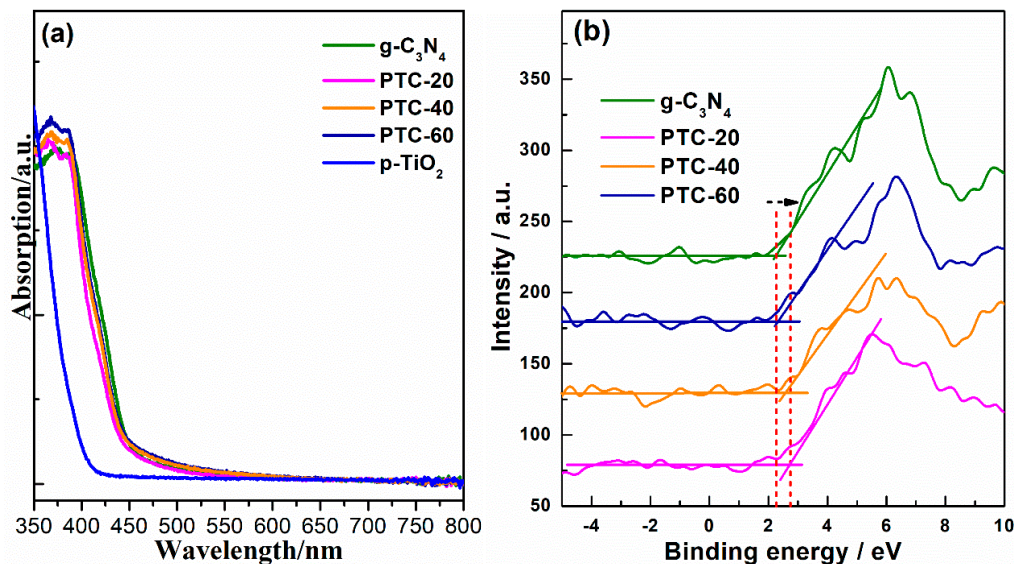
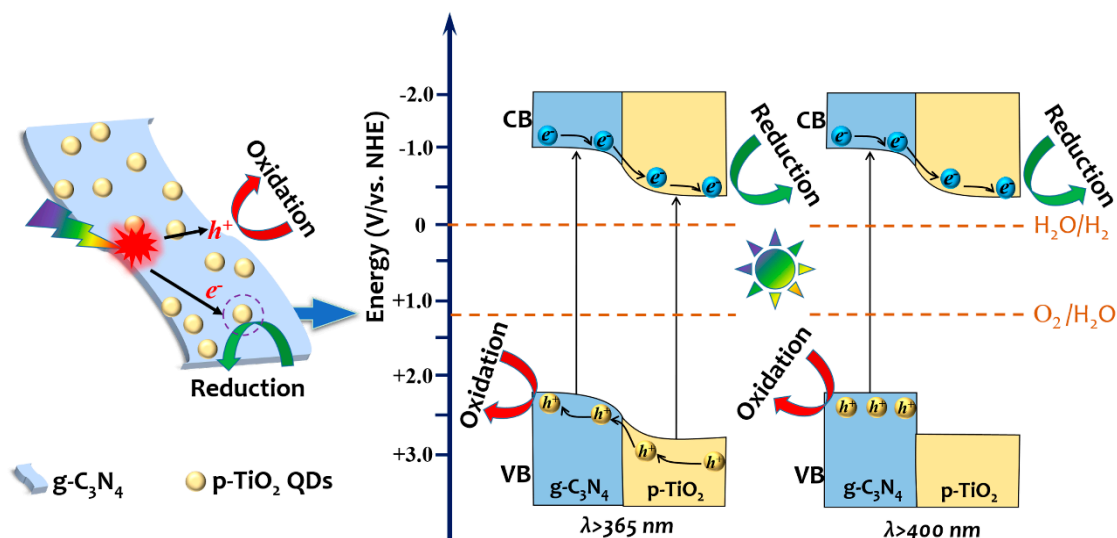


Figure 7. (a) UV-vis DRS spectra and (b) valence band density of states (DOS) of layered g-C₃N₄, PTC-20, PTC-40 and PTC-60.

As mentioned above, we have demonstrated that the surface deposited TiO₂ QDs is abundant in titanium vacancies, while both experimental and density functional theoretical (DFT) results have indicated that metal defected TiO₂ is p-type semiconductor [28]. In general, g-C₃N₄ exhibits n-type conductivity, therefore, p-n heterojunctions will be formed across the interface, which can afford a large electrical field and more efficient charge separation. Therefore, according to the band gap and valence band (VB) position of pure g-C₃N₄ and TiO₂, the band alignment of the p-n heterojunction (PTC-40) is diagrammed in Scheme 2. Both TiO₂ and g-C₃N₄ can be excited under $\lambda > 365$ nm, charge redistribution process will occur to equilibrate the Fermi level (E_f) due to the large difference of E_f between p-type TiO₂ and n-type g-C₃N₄, the consequence is that the photogenerated electrons migrate to the conduction band (CB) of TiO₂ and holes to the g-C₃N₄ VB. However, only g-C₃N₄ can be excited under visible light irradiation ($\lambda > 400$ nm), and the photogenerated electrons will still transfer to the CB of TiO₂, while the holes tend to keep stay in the VB of g-C₃N₄. In both cases, an efficient electron-hole spatial separation can be realized and the lifetime of charge carriers can also be prolonged, these separated electrons can react with O₂ or H₂O to form reactive oxygen species ($\cdot\text{O}_2^-$) or H₂, while the holes will oxidize an organic pollutant or sacrificial agent directly. In addition, the presence of metal vacancies will enlarge the width of VB, which controls the mobility of holes inherently [28], and thus the synergy influence of metal vacancies, quantum confinement effect, and nanosheet structure can effectively promote the charge transfer and separation across the interface.

The facilitated charge separation by the p-n heterojunction was confirmed by photoluminescence (PL) spectra. As shown in Figure 8, pure g-C₃N₄ has an emission peak around 450 nm, whereas p-TiO₂ exhibits a signal at around 400nm, which is due to the band-band transition, namely the energy corresponding to the emission is close to the excitation energy of g-C₃N₄ and TiO₂, respectively [25,29]. The PL intensity of PTC-*x* is much lower than pure p-type TiO₂ and g-C₃N₄, indicating a promoted electron-hole separation by the p-n heterojunction. Notably, PTC-40 exhibits the lowest PL intensity among the samples, suggesting a higher charge separation efficiency and a better photocatalytic performance, which also indicates that there exists an approximate p/n ratio between the p-type TiO₂ and n-type g-C₃N₄ in the heterojunction.



Scheme 2. Schematic illustration of TiO₂ QDs@g-C₃N₄ p-n heterojunction and the pathway for electron-hole transfer and separation over the junction under simulated solar irradiation ($\lambda > 365$ nm) and visible light irradiation ($\lambda > 400$ nm).

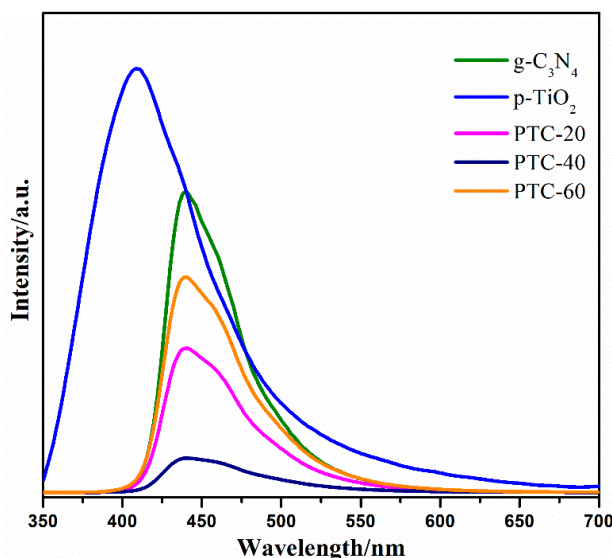


Figure 8. Steady state PL spectra of layered g-C₃N₄, PTC-20, PTC-40 and PTC-60.

Photocatalytic degradation of organic pollutants and photocatalytic water splitting were conducted to evaluate the performance of as-prepared TiO₂@g-C₃N₄ p-n heterojunctions. Figure 9a shows the photodegradation rate of the samples based on pseudo-first-order reaction mode. Under simulated sunlight irradiation ($\lambda > 365$ nm), the degradation rate of MO for PTC-40 with a TiO₂ (p) to g-C₃N₄ (n) mass ratio of 0.15 is $0.52 \text{ min}^{-1} \cdot \text{g}^{-1}$, which is the highest among the PTC-*x* and is 4.3-fold higher than that of pure g-C₃N₄. Moreover, we also tested the photoactivity with a cut-off filter of $\lambda > 400$ nm to evaluate the visible light photocatalytic performance, the reaction rate exhibits the same trends with that under simulated solar spectrum (Figure 9b), and the reaction rate for MO degradation of PTC-40 is $0.125 \text{ min}^{-1} \cdot \text{g}^{-1}$, 5.4-fold higher than pure g-C₃N₄. This result confirms that p-n heterojunction exhibits a better photocatalytic performance than single photocatalyst and that the as-prepared TiO₂@g-C₃N₄ is active under visible light.

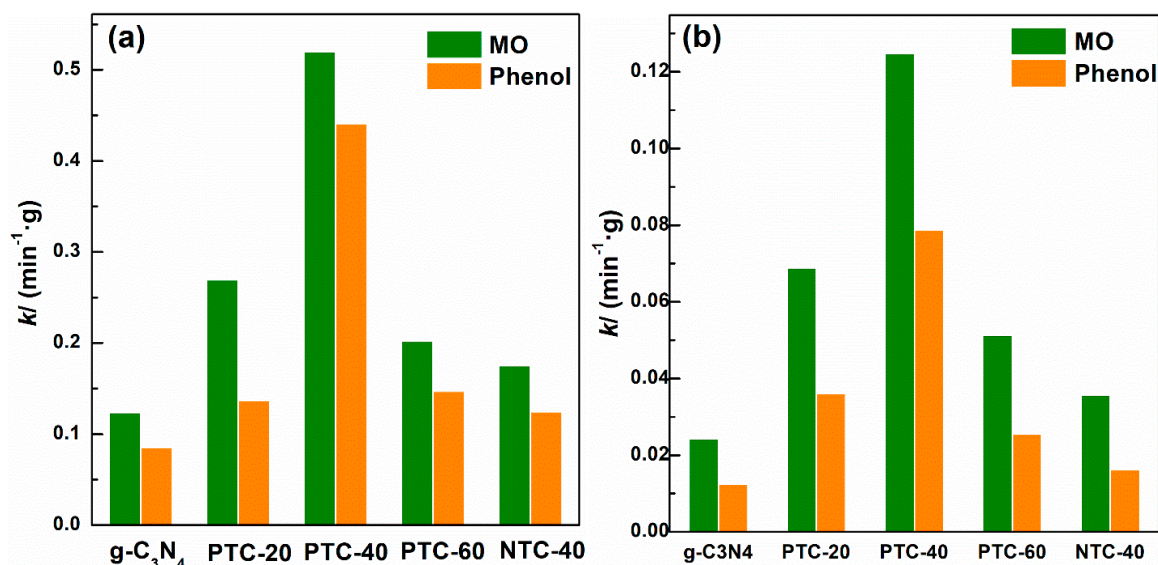


Figure 9. Pseudo-first-order reaction rate in degradation of methyl orange (MO) and phenol under: (a) full solar spectrum and (b) visible light ($\lambda > 400$ nm).

The photocatalytic H₂ evolution reaction rate is shown in Figure 10a, the H₂ release rate for g-C₃N₄, PTC-20, PTC-40 and PTC-60 is 186 $\mu\text{mol}\cdot\text{g}^{-1}\cdot\text{h}^{-1}$, 712 $\mu\text{mol}\cdot\text{g}^{-1}\cdot\text{h}^{-1}$, 1072 $\mu\text{mol}\cdot\text{g}^{-1}\cdot\text{h}^{-1}$ and 838 $\mu\text{mol}\cdot\text{g}^{-1}\cdot\text{h}^{-1}$, respectively. It is clearly that the H₂ evolution rate of PTC-40 is the fastest, which is 5.8-fold of pure g-C₃N₄, 1.5-fold of PTC-20 and 1.3-fold of PTC-60. Combining with the PL results and photoactivity, we can get the conclusion that PTC-40 has the most efficient electron-hole separation, and thus exhibits the best photocatalytic performance among the as-fabricated samples. Meanwhile, this phenomenon also indicates that a suitable p/n ratio is required to construct the best p-n heterojunction. In comparison, we also loaded n-type TiO₂ QDs on the surface of g-C₃N₄ to construct a type-II heterojunction and found that the promotion in photoactivity is far from that by p-n heterojunction (1.44-fold vs. 5.8-fold in H₂ evolution), illustrating that p-n heterojunctions are more effective in accelerating photogenerated charge carrier separation and promoting the photocatalytic performance.

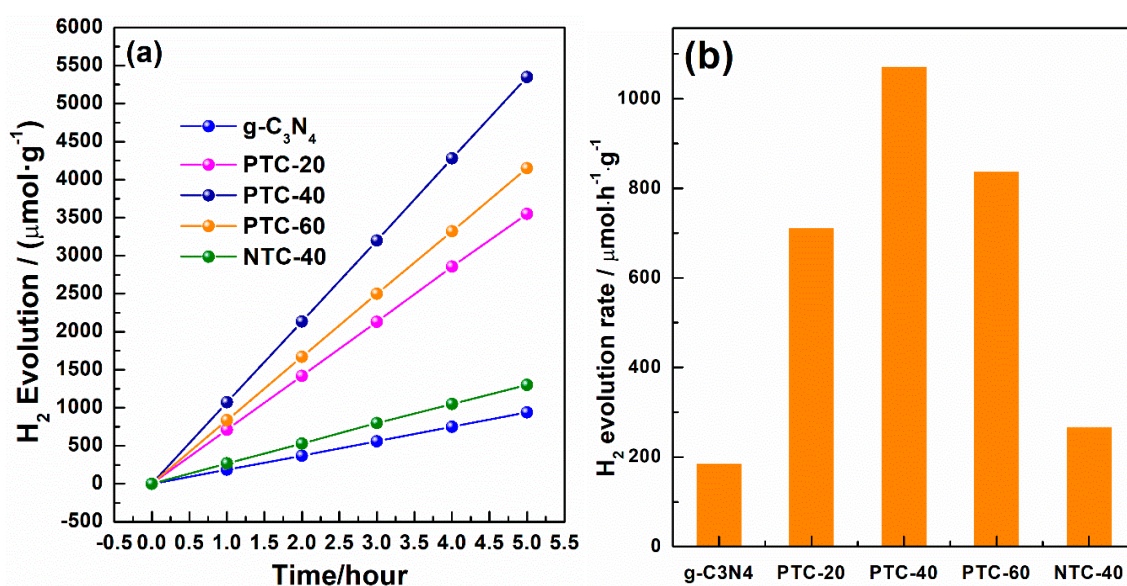


Figure 10. (a) Time course of hydrogen evolution and (b) hydrogen generation rate of the samples.

3. Experimental

3.1. Materials

Ethanol, glycerol, melamine and methyl orange (MO) were all purchased from Tianjin Jiangtian Fine Chemical Research Institute. Titanium butoxide ($C_{16}H_{36}O_4Ti$, TBOT), triethanolamine (TEOA) and phenol were purchased from J&K chemical. Milli-Q ultra-pure water with a resistivity larger than $18.2 M\Omega\cdot cm$ was used in all experiments. All the chemicals were reagent grade and used as received.

3.2. Preparation of Bulk $g-C_3N_4$

Bulk $g-C_3N_4$ was synthesized by thermal annealing melamine under air atmosphere. Typically, 5 g of melamine was put into an airtight crucible, then the crucible was placed into a muffle furnace and calcined at $550\text{ }^\circ C$ for 4 h with a ramping rate of $5\text{ }^\circ C/min$. After being cooled down to room temperature naturally, the obtained yellow powder is bulk $g-C_3N_4$.

3.3. Preparation of TiO_2 QDs@ $g-C_3N_4$ p-n Heterojunction

As shown in Scheme 1, for the fabrication of TiO_2 QDs@ $g-C_3N_4$ p-n heterojunction, x ($x = 20, 40, 60$) mg $g-C_3N_4$ was dispersed in 148 mL ethanol and sonicated for one hour. After that, 5 mL glycerol was added into the solution. After being stirred for another 20 min, 400 μL TBOT was dropwisely into the solution and then titanium glycerolate (TiGly) was in-situ grown on the surface of $g-C_3N_4$, the solution was stirred at room temperature for 16 h. The resulted powders (labeled as TGC- x) were washed with water and absolute ethanol for several times, and dried at $70\text{ }^\circ C$ overnight. After calcination of TGC- x in air at $470\text{ }^\circ C$ for 1 h, TiO_2 QDs@ $g-C_3N_4$ p-n heterojunctions were obtained and labeled as PTC- x ($x = 20, 40, 60$). As a reference, n-type TiO_2 QDs deposited $g-C_3N_4$ was synthesized with the same procedure ($x = 40$ mg) except that glycerol was replaced by 233 μL $NH_3\cdot H_2O$ for the purpose of triggering the nucleation of TiO_2 on $g-C_3N_4$ as previously reported (the reference sample was labeled as NTC-40) [29].

3.4. Characterization of Photocatalysts

The calcination temperature for the decomposition of titanium glycerolate and the content of TiO_2 was determined by thermogravimetric analysis (TGA Q500, TA Instruments, DE, USA) with air gas flow at 50 mL/min in a range of $30\text{--}500\text{ }^\circ C$ ($5\text{ }^\circ C/min$). In order to obtain the composition of the samples, Fourier transform infrared spectroscopy (FT-IR, Bruker Tensor-27 spectrum, Bavaria, Germany) was conducted before and after calcination, the FT-IR spectra were acquired in the range of $400\text{--}4000\text{ cm}^{-1}$ with a resolution of 1 cm^{-1} .

All the samples were characterized with an X-ray diffractometer (XRD-6100, Shimadzu, Kyoto, Japan) to determine the crystalline properties. The X-ray diffractometer was equipped with a $Cu\ K\alpha$ radiation at 40 kV and 30 mA at a scanning rate of $5^\circ/min$. The diffraction patterns were determined over 2 theta range of $5^\circ\text{--}90^\circ$ with a resolution of $2^\circ/min$. To obtain the average size of the crystalline size, Scherrer equation was used ($D = 0.9\lambda/\beta\cos\theta$), whereas the lattice constants was calculated according to Bragg equation of $2dhklsin\theta = \lambda$, where λ is the applied wavelength, θ is the Bragg angle and β is the FWHM value.

The chemical states of the as-prepared samples were characterized by X-ray photoelectron spectroscopy (PHI-1600, ULVAC-PHI, Kanagawa, Japan) with $Al\ K\alpha$ radiation, and the binding energy was calibrated by the $C1s$ peak (284.8 eV) of the contamination carbon. High resolution transmission electron microscopy (HRTEM) analysis was carried out using a Tecnai G^2 F-20 transmission electron microscope (FEI, OR, USA) with a field-emission gun operation at 200 kV.

The band gap and the light absorption properties of the samples were determined with a UV-vis diffuse reflectance spectrum (U-3010, Hitachi Ltd., Lbarakiken, Japan) with a 60 mm diameter integrating sphere using $BaSO_4$ as the reflectance sample. Steady-state photoluminescence spectra (PL) spectra were measured by a Fluorolog3-21 (Horiba JobinYvon, NJ, USA) with the excitation light at 325 nm.

3.5. Photocatalytic Degradation and Hydrogen Evolution

Photodegradation of organic pollutants (phenol and MO) was conducted in an opening quartz chamber (150 mL) vertically irradiated by a 300 W high-pressure xenon lamp (PLS-SXE300, Beijing Perfect Light Co. Ltd., Beijing, China) located on the upper position. The irradiation area was about 20 cm². The light density was measured using a radiometer (Photoelectric Instrument Factory, Beijing Normal University, Model UV-A, Beijing, China), and the results indicate that the light density at 365 nm and 400 nm was 34.7 mW/cm² and 32.5 mW/cm², respectively. Reaction conditions included the following: a temperature of 25 °C, solution volume of 100 mL, C₀ (phenol) of 400 μmol·L⁻¹; C₀ (MO) of 120 μmol·L⁻¹; photocatalyst of 0.1 g·L⁻¹. Prior to the reaction, the suspension was stirred without irradiation for 20 min to achieve an adsorption equilibrium. Samples were withdrawn, centrifuged and analyzed using a U-3010 UV-vis spectrometer.

Photocatalytic hydrogen production was carried out in a Pyrex top-irradiation reaction vessel connected to closed glass gas system. 10 mg catalyst dispersed in 120 mL aqueous solution containing TEOA (30 vol.%). The temperature of reaction solution was maintained at 0 °C. The resultant hydrogen was analyzed using an off-line gas chromatography (Bruker 450-GC, CA, USA) equipped with a thermal conductive detector (TCD), 5 Å molecular sieve column, and N₂ as carrier gas.

4. Conclusions

In this work, p-TiO₂ QDs@g-C₃N₄ p-n heterojunctions were fabricated by in-situ decorating titanium-defected TiO₂ QDs on the surface of g-C₃N₄, in which TiO₂ QDs bring up p-type conductivity and g-C₃N₄ affords for n-type conductivity. The as-prepared p-n heterojunction exhibits higher charge separation efficiency and photocatalytic performance in H₂ evolution reaction and degradation of organic pollutant than pure g-C₃N₄ and TiO₂/g-C₃N₄ type-II heterojunction under both UV-light and visible light irradiation, which can be ascribed to the synergy of a large electrical field over interface, a strong interface interaction, and the quantum confinement effect. In all the samples, PTC-40 with a p/n mass ratio of 0.15 exhibits the best photocatalytic performance. This work demonstrates that the construction of p-n heterojunction is an effective pathway to accelerate the electron-hole separation that is the key for a highly efficient photocatalyst.

Author Contributions: Conceptualization, N.T. and S.W.; methodology, L.Z., W.D. and J.X.; formal analysis, F.W.; investigation, S.W. and F.W.; data curation, F.W., Z.S., X.W. and Y.H.; writing—original draft preparation, F.W.; writing—review and editing, S.W.

Funding: This research was funded by the National Natural Science Foundation of China (No. 21808172), Tianjin Municipal Natural Science Foundation (No. 18JCQNJC05800, 18JCZDJC37200), Innovation Fund for Young Talents of TUST and the foundation of Tianjin Key Laboratory of Marine Resources and Chemistry (TUST, No. 201707).

Conflicts of Interest: The authors declare no conflict of interest.

References

1. Fujishima, A.; Honda, K. Electrochemical Photolysis of Water at a Semiconductor Electrode. *Nature* **1972**, *238*, 37–38. [[CrossRef](#)]
2. Wu, S.-M.; Liu, X.-L.; Lian, X.-L.; Tian, G.; Janiak, C.; Zhang, Y.-X.; Lu, Y.; Yu, H.-Z.; Hu, J.; Wei, H.; et al. Homojunction of Oxygen and Titanium Vacancies and its Interfacial n-p Effect. *Adv. Mater.* **2018**, *30*, 1802173. [[CrossRef](#)]
3. Zhang, N.; Yang, M.-Q.; Liu, S.; Sun, Y.; Xu, Y.-J. Waltzing with the Versatile Platform of Graphene to Synthesize Composite Photocatalysts. *Chem. Rev.* **2015**, *115*, 10307–10377. [[CrossRef](#)] [[PubMed](#)]
4. Wondraczek, L.; Tyystjärvi, E.; Méndez-Ramos, J.; Müller, F.A.; Zhang, Q. Shifting the Sun: Solar Spectral Conversion and Extrinsic Sensitization in Natural and Artificial Photosynthesis. *Adv. Sci.* **2015**, *2*, 1500218. [[CrossRef](#)]
5. Zhang, H.; Liu, G.; Shi, L.; Liu, H.; Wang, T.; Ye, J. Engineering coordination polymers for photocatalysis. *Nano Energy* **2016**, *22*, 149–168. [[CrossRef](#)]

6. Kapilashrami, M.; Zhang, Y.; Liu, Y.-S.; Hagfeldt, A.; Guo, J. Probing the Optical Property and Electronic Structure of TiO₂ Nanomaterials for Renewable Energy Applications. *Chem. Rev.* **2014**, *114*, 9662–9707. [[CrossRef](#)] [[PubMed](#)]
7. Fresno, F.; Portela, R.; Suárez, S.; Coronado, J.M. Photocatalytic materials: recent achievements and near future trends. *J. Mater. Chem. A* **2014**, *2*, 2863–2884. [[CrossRef](#)]
8. Chen, X.; Mao, S.S. Titanium Dioxide Nanomaterials: Synthesis, Properties, Modifications, and Applications. *Chem. Rev.* **2007**, *107*, 2891–2959. [[CrossRef](#)] [[PubMed](#)]
9. Pan, X.; Yang, M.-Q.; Fu, X.; Zhang, N.; Xu, Y.-J. Defective TiO₂ with oxygen vacancies: synthesis, properties and photocatalytic applications. *Nanoscale* **2013**, *5*, 3601–3614. [[CrossRef](#)]
10. Ma, Y.; Wang, X.; Jia, Y.; Chen, X.; Han, H.; Li, C. Titanium Dioxide-Based Nanomaterials for Photocatalytic Fuel Generations. *Chem. Rev.* **2014**, *114*, 9987–10043. [[CrossRef](#)]
11. Wang, Z.; Yang, C.; Lin, T.; Yin, H.; Chen, P.; Wan, D.; Xu, F.; Huang, F.; Lin, J.; Xie, X.; et al. Visible-light photocatalytic, solar thermal and photoelectrochemical properties of aluminium-reduced black titania. *Energy Environ. Sci.* **2013**, *6*, 3007–3014. [[CrossRef](#)]
12. Yang, H.G.; Sun, C.H.; Qiao, S.Z.; Zou, J.; Liu, G.; Smith, S.C.; Cheng, H.M.; Lu, G.Q. Anatase TiO₂ single crystals with a large percentage of reactive facets. *Nature* **2008**, *453*, 638. [[CrossRef](#)]
13. Li, L.; Yan, J.; Wang, T.; Zhao, Z.J.; Zhang, J.; Gong, J.; Guan, N. Sub-10 nm rutile titanium dioxide nanoparticles for efficient visible-light-driven photocatalytic hydrogen production. *Nat. Commun.* **2015**, *6*, 5881. [[CrossRef](#)] [[PubMed](#)]
14. Liu, G.; Yang, H.G.; Pan, J.; Yang, Y.Q.; Lu, G.Q.; Cheng, H.-M. Titanium Dioxide Crystals with Tailored Facets. *Chem. Rev.* **2014**, *114*, 9559–9612. [[CrossRef](#)] [[PubMed](#)]
15. Di Valentin, C.; Pacchioni, G.; Selloni, A. Reduced and n-Type Doped TiO₂: Nature of Ti³⁺ Species. *J. Phys. Chem. C* **2009**, *113*, 20543–20552. [[CrossRef](#)]
16. Livraghi, S.; Paganini, M.C.; Giamello, E.; Selloni, A.; Di Valentin, C.; Pacchioni, G. Origin of Photoactivity of Nitrogen-Doped Titanium Dioxide under Visible Light. *J. Am. Chem. Soc.* **2006**, *128*, 15666–15671. [[CrossRef](#)]
17. Li, J.-G.; Büchel, R.; Isobe, M.; Mori, T.; Ishigaki, T. Cobalt-Doped TiO₂ Nanocrystallites: Radio-Frequency Thermal Plasma Processing, Phase Structure, and Magnetic Properties. *J. Phys. Chem. C* **2009**, *113*, 8009–8015. [[CrossRef](#)]
18. Cao, J.; Zhang, Y.; Liu, L.; Ye, J. A p-type Cr-doped TiO₂ photo-electrode for photo-reduction. *Chem. Commun.* **2013**, *49*, 3440–3442. [[CrossRef](#)]
19. Wang, Y.; Han, P.; Lv, X.; Zhang, L.; Zheng, G. Defect and Interface Engineering for Aqueous Electrocatalytic CO₂ Reduction. *Joule* **2018**, *2*, 2551–2582. [[CrossRef](#)]
20. Wang, T.; Liu, L.; Ge, G.; Liu, M.; Zhou, W.; Chang, K.; Yang, F.; Wang, D.; Ye, J. Two-dimensional titanium oxide nanosheets rich in titanium vacancies as an efficient cocatalyst for photocatalytic water oxidation. *J. Catal.* **2018**, *367*, 296–305. [[CrossRef](#)]
21. Nowotny, M.K.; Bogdanoff, P.; Dittrich, T.; Fiechter, S.; Fujishima, A.; Tributsch, H. Observations of p-type semiconductivity in titanium dioxide at room temperature. *Mater. Lett.* **2010**, *64*, 928–930. [[CrossRef](#)]
22. Wu, Q.; Huang, F.; Zhao, M.; Xu, J.; Zhou, J.; Wang, Y. Ultra-small yellow defective TiO₂ nanoparticles for co-catalyst free photocatalytic hydrogen production. *Nano Energy* **2016**, *24*, 63–71. [[CrossRef](#)]
23. Dahl, M.; Liu, Y.; Yin, Y. Composite Titanium Dioxide Nanomaterials. *Chem. Rev.* **2014**, *114*, 9853–9889. [[CrossRef](#)] [[PubMed](#)]
24. Li, H.; Zhou, Y.; Tu, W.; Ye, J.; Zou, Z. State-of-the-Art Progress in Diverse Heterostructured Photocatalysts toward Promoting Photocatalytic Performance. *Adv. Funct. Mater.* **2015**, *25*, 998–1013. [[CrossRef](#)]
25. Tong, Z.; Yang, D.; Xiao, T.; Tian, Y.; Jiang, Z. Biomimetic fabrication of g-C₃N₄/TiO₂ nanosheets with enhanced photocatalytic activity toward organic pollutant degradation. *Chem. Eng. J.* **2015**, *260*, 117–125. [[CrossRef](#)]
26. Wang, S.; Huang, C.-Y.; Pan, L.; Chen, Y.; Zhang, X.; Fazale, A.; Zou, J.-J. Controllable fabrication of homogeneous ZnO p-n junction with enhanced charge separation for efficient photocatalysis. *Catal. Today* **2018**. [[CrossRef](#)]
27. Wang, M.; Sun, L.; Lin, Z.; Cai, J.; Xie, K.; Lin, C. p-n Heterojunction photoelectrodes composed of Cu₂O-loaded TiO₂ nanotube arrays with enhanced photoelectrochemical and photoelectrocatalytic activities. *Energy Environ. Sci.* **2013**, *6*, 1211–1220. [[CrossRef](#)]

28. Wang, S.; Pan, L.; Song, J.-J.; Mi, W.; Zou, J.-J.; Wang, L.; Zhang, X. Titanium-Defected Undoped Anatase TiO₂ with p-Type Conductivity, Room-Temperature Ferromagnetism, and Remarkable Photocatalytic Performance. *J. Am. Chem. Soc.* **2015**, *137*, 2975–2983. [[CrossRef](#)]
29. Pan, L.; Wang, S.; Xie, J.; Wang, L.; Zhang, X.; Zou, J.-J. Constructing TiO₂ p-n homojunction for photoelectrochemical and photocatalytic hydrogen generation. *Nano Energy* **2016**, *28*, 296–303. [[CrossRef](#)]
30. Ma, L.; Han, H.; Pan, L.; Tahir, M.; Wang, L.; Zhang, X.; Zou, J.-J. Fabrication of TiO₂ nanosheets via Ti³⁺ doping and Ag₃PO₄ QD sensitization for highly efficient visible-light photocatalysis. *RSC Adv.* **2016**, *6*, 63984–63990. [[CrossRef](#)]
31. Pan, L.; Zou, J.-J.; Wang, S.; Huang, Z.-F.; Yu, A.; Wang, L.; Zhang, X. Quantum dot self-decorated TiO₂ nanosheets. *Chem. Commun.* **2013**, *49*, 6593–6595. [[CrossRef](#)]
32. Anpo, M.; Kawamura, T.; Kodama, S.; Maruya, K.; Onishi, T. Photocatalysis on titanium-aluminum binary metal oxides: enhancement of the photocatalytic activity of titania species. *J. Phys. Chem.* **1988**, *92*, 438–440. [[CrossRef](#)]
33. Cao, S.; Yu, J. g-C₃N₄-Based Photocatalysts for Hydrogen Generation. *J. Phys. Chem. Lett.* **2014**, *5*, 2101–2107. [[CrossRef](#)] [[PubMed](#)]
34. Wang, X.; Blechert, S.; Antonietti, M. Polymeric Graphitic Carbon Nitride for Heterogeneous Photocatalysis. *ACS Catal.* **2012**, *2*, 1596–1606. [[CrossRef](#)]
35. Low, J.; Cao, S.; Yu, J.; Wageh, S. Two-dimensional layered composite photocatalysts. *Chem. Commun.* **2014**, *50*, 10768–10777. [[CrossRef](#)]
36. Butchosa, C.; Guiglion, P.; Zwijnenburg, M.A. Carbon Nitride Photocatalysts for Water Splitting: A Computational Perspective. *J. Phys. Chem. C* **2014**, *118*, 24833–24842. [[CrossRef](#)]
37. Zhang, H.; Zuo, X.; Tang, H.; Li, G.; Zhou, Z. Origin of photoactivity in graphitic carbon nitride and strategies for enhancement of photocatalytic efficiency: insights from first-principles computations. *Phys. Chem. Chem. Phys.* **2015**, *17*, 6280–6288. [[CrossRef](#)]
38. Huang, Z.-F.; Song, J.; Pan, L.; Wang, Z.; Zhang, X.; Zou, J.-J.; Mi, W.; Zhang, X.; Wang, L. Carbon nitride with simultaneous porous network and O-doping for efficient solar-energy-driven hydrogen evolution. *Nano Energy* **2015**, *12*, 646–656. [[CrossRef](#)]
39. Zhang, J.-W.; Gong, S.; Mahmood, N.; Pan, L.; Zhang, X.; Zou, J.-J. Oxygen-doped nanoporous carbon nitride via water-based homogeneous supramolecular assembly for photocatalytic hydrogen evolution. *Appl. Catal. B-Environ.* **2018**, *221*, 9–16. [[CrossRef](#)]
40. Ye, C.; Li, J.-X.; Li, Z.-J.; Li, X.-B.; Fan, X.-B.; Zhang, L.-P.; Chen, B.; Tung, C.-H.; Wu, L.-Z. Enhanced Driving Force and Charge Separation Efficiency of Protonated g-C₃N₄ for Photocatalytic O₂ Evolution. *ACS Catal.* **2015**, *5*, 6973–6979. [[CrossRef](#)]
41. Zhang, S.; Li, J.; Wang, X.; Huang, Y.; Zeng, M.; Xu, J. Rationally designed 1D Ag@AgVO₃ nanowire/graphene/protonated g-C₃N₄ nanosheet heterojunctions for enhanced photocatalysis via electrostatic self-assembly and photochemical reduction methods. *J. Mater. Chem. A* **2015**, *3*, 10119–10126. [[CrossRef](#)]
42. Yang, S.B.; Gong, Y.J.; Zhang, J.S.; Zhan, L.; Ma, L.L.; Fang, Z.Y.; Vajtai, R.; Wang, X.C.; Ajayan, P.M. Exfoliated Graphitic Carbon Nitride Nanosheets as Efficient Catalysts for Hydrogen Evolution Under Visible Light. *Adv. Mater.* **2013**, *25*, 2452–2456. [[CrossRef](#)]
43. Niu, P.; Zhang, L.L.; Liu, G.; Cheng, H.M. Graphene-Like Carbon Nitride Nanosheets for Improved Photocatalytic Activities. *Adv. Funct. Mater.* **2012**, *22*, 4763–4770. [[CrossRef](#)]
44. Xu, H.; Yan, J.; She, X.; Xu, L.; Xia, J.; Xu, Y.; Song, Y.; Huang, L.; Li, H. Graphene-analogue carbon nitride: novel exfoliation synthesis and its application in photocatalysis and photoelectrochemical selective detection of trace amount of Cu²⁺. *Nanoscale* **2014**, *6*, 1406–1415. [[CrossRef](#)]
45. Kang, Y.; Yang, Y.; Yin, L.-C.; Kang, X.; Liu, G.; Cheng, H.-M. An Amorphous Carbon Nitride Photocatalyst with Greatly Extended Visible-Light-Responsive Range for Photocatalytic Hydrogen Generation. *Adv. Mater.* **2015**, *27*, 4572–4577. [[CrossRef](#)]
46. Jun, Y.-S.; Lee, E.Z.; Wang, X.; Hong, W.H.; Stucky, G.D.; Thomas, A. From Melamine-Cyanuric Acid Supramolecular Aggregates to Carbon Nitride Hollow Spheres. *Adv. Funct. Mater.* **2013**, *23*, 3661–3667. [[CrossRef](#)]
47. Liang, Q.; Li, Z.; Yu, X.; Huang, Z.-H.; Kang, F.; Yang, Q.-H. Macroscopic 3D Porous Graphitic Carbon Nitride Monolith for Enhanced Photocatalytic Hydrogen Evolution. *Adv. Mater.* **2015**, *27*, 4634–4639. [[CrossRef](#)]

48. Zhang, J.; Zhang, M.; Lin, L.; Wang, X. Sol Processing of Conjugated Carbon Nitride Powders for Thin-Film Fabrication. *Angew. Chem. Int. Edit.* **2015**, *54*, 6297–6301. [[CrossRef](#)]
49. Das, J.; Freitas, F.S.; Evans, I.R.; Nogueira, A.F.; Khushalani, D. A facile nonaqueous route for fabricating titania nanorods and their viability in quasi-solid-state dye-sensitized solar cells. *J. Mater. Chem.* **2010**, *20*, 4425–4431. [[CrossRef](#)]



© 2019 by the authors. Licensee MDPI, Basel, Switzerland. This article is an open access article distributed under the terms and conditions of the Creative Commons Attribution (CC BY) license (<http://creativecommons.org/licenses/by/4.0/>).